

Aerosol physicochemical properties and implication of visibility during an intense haze episode during winter in Beijing

Y. H. Wang^{1,2}, Z. R. Liu¹, J. K. Zhang¹, B. Hu¹, D. S. Ji¹, Y. C. Yu¹ and Y. S. Wang^{1,2}

1 State Key Laboratory of Atmospheric Boundary Layer Physics and Atmospheric Chemistry (LAPC), Institute of Atmospheric Physics, Chinese Academy of Sciences, Beijing 100029, China

2 College of Atmospheric Sciences, Lanzhou University, Lanzhou, 730000, China

*Corresponding Author: Y. S. Wang

Email: wys@mail.iap.ac.cn

1 Abstract

2 The evolution of physical, chemical and optical properties of urban aerosol particles
3 was characterized during an **extremely** haze episode in Beijing, PRC, from January 24
4 through January 31, 2013 based on in-situ measurements. The average mass
5 concentrations of PM₁ (**particle aerodynamic diameter no more than 1 micrometer**),
6 PM_{2.5} (**particle aerodynamic diameter no more than 1 micrometer**) and PM₁₀ (**particle**
7 **aerodynamic diameter no more than 1 micrometer**) were $99 \pm 67 \mu\text{g m}^{-3}$ (average \pm
8 stdev), $188 \pm 128 \mu\text{g m}^{-3}$ and $265 \pm 157 \mu\text{g m}^{-3}$, respectively. A significant increase in
9 PM_{1-2.5} fraction was observed during the most heavily polluted **period**. The average
10 scattering coefficient **at 550 nm** was $877 \text{ Mm}^{-1} \pm 624 \text{ Mm}^{-1}$. An increasing relative
11 amount of coarse particles can be deduced from the variations of backscattering ratios,
12 asymmetry parameter and scattering Ångström exponent. Particle number size
13 distributions between 14 nm-2500 nm diameter showed high number concentrations,
14 particularly in the nucleation mode and accumulation **mode**. Size-resolved chemical
15 composition of submicron aerosol from a High Resolution-ToF-Aerosol Mass
16 Spectrometer showed that the mass **concentrations** of organic, sulfate, nitrate,
17 ammonium and chlorine mainly resided on 500nm to 800nm (vacuum diameter)
18 particles, **and nitrate and ammonium contributed greatly to particle growth during the**
19 **heavily polluted day (January 28)**.
20 Increasing relative humidity and stable synoptic conditions on January 28 combined
21 with heavy pollution **on 28 January**, lead to enhanced water uptake by the hygroscopic
22 submicron particles and formation of secondary aerosol, **which might** be the main

23 reasons for the severity of the haze episode. Light scattering apportionment showed
24 that organic, **sulfate**, ammonium nitrate and ammonium chloride compounds
25 contributed to light scattering fractions of **54%, 24%, 12% and 10%**, respectively.
26 This study indicated that the organic component in submicron aerosol **played** an
27 important role in visibility degradation **during the haze episode in Beijing**.

28 **1. Introduction**

29 Atmospheric aerosol particles play **a** significant role in radiation balance and climate
30 forcing through direct scattering and absorption of solar radiation (Anderson et al.,
31 2003; Poschl, 2005; Ramanathan et al., 2001). **In addition**, they can act as cloud
32 condensation nuclei (CCN) and thereby change the cloud albedo and lifetime (Twomey,
33 1977). Accordingly, the radiative properties of clouds are **indirectly** influenced by
34 aerosol (Kaufman et al., 2005; Koren et al., 2005; Lohmann and Feichter, 2005).
35 Furthermore, the general public has to pay special attention to atmospheric aerosol due
36 to its deleterious **effect** on human health and degradation of visibility (Nel, 2005;
37 Watson, 2002), which are closely related to the chemical components, morphology,
38 mixing state, size distribution and hygroscopic properties of aerosol particles.
39 Along with the rapid economic growth in China, its capital city Beijing has suffered
40 substantially from air quality deterioration and visibility degradation, **though the mass**
41 **concentration of PM₁₀ has decreased** in Beijing in the last ten years (Liu et al., 2015).
42 Accompanied by frequent fog-haze days, the visibility in Beijing has decreased
43 dramatically to an unacceptable level. The **frequency of visibility** between 2km and

44 10km has increased from 37% in 1999 to 43% in 2007. (Zhang et al., 2010; Zhang et
45 al., 2012). The mass loading of fine aerosol particles and their precursors (e.g. NH₃,
46 volatile organic compounds (VOCs), SO₂ and NO_x), can accumulate to high levels
47 within the planetary boundary layer , especially during persistent synoptic stagnation
48 and strong temperature inversion (Zhang et al., 2013). In the past decade, many
49 researches have been done to characterize the chemical and physical properties of
50 aerosol particles in Beijing and its surrounding regions. These studies mainly focused
51 on the following aspects:

- 52 i) Chemical composition, evaluation and sources apportionment based on filter
53 sampling and Aerosol Mass Spectrometry (AMS) (Huang et al., 2010b; Sun et
54 al., 2006; Zhang et al., 2014) .
- 55 ii) Mass concentration and optical properties of aerosol particles using in-situ
56 measurements or combined with MODIS (Moderate Resolution Imaging
57 Spectroradiometer) satellite remote sensing optical depth products (He et al.,
58 2009; Huang et al., 2010a; Li et al., 2010; Qu et al., 2010; Wang et al., 2012a;
59 Yang et al., 2009).
- 60 iii) Aerosol hygroscopic properties, number size distributions, mixing state and
61 implications for CCN activity, visibility, new particle formation, air pollution
62 and radiative forcing (Chen et al., 2012; Cheng et al., 2012; Deng et al., 2013;
63 Liu et al., 2013; Ma et al., 2012; Meier et al., 2009; Pan et al., 2009; Quan et al.,
64 2011; Wehner et al., 2008; Wu et al., 2007; Zhang et al., 2011; Zhang et al.,
65 2010).

66 The above mentioned studies, based on either long-term or short-term observations
67 provide us with comprehensive knowledge of aerosol properties on days with near
68 average aerosol concentration levels. However, only a few studies were carried out
69 under highly polluted days, and these studies mainly focus on variations of chemical
70 composition with the evaluation of synoptic conditions and planetary boundary layer
71 dynamics. (Huang et al., 2010a; Wang et al., 2012b; Zhao et al., 2013). The interaction
72 between chemical and physical properties of aerosol was seldom investigated during
73 haze episodes. Therefore, comprehensive studies of physical, optical and chemical
74 properties using high resolution measurements are necessary for a better knowledge of
75 aerosol evolution processes and related visibility degradation during pollution episodes
76 in Beijing.

77 An intense pollution episode occurred in central and eastern China from January 24
78 through 31, 2013. The hourly average PM₁₀ exceeded 600 µg m⁻³ and non-refractory
79 submicron particle (NR-PM₁) exceeded 400 µg m⁻³ (Wang et al., 2013), which was the
80 most extreme haze episode in Beijing in the last decades as far as we know. In this
81 study, we investigated the evolution of physical, chemical, and optical properties of
82 urban aerosol particle during the haze episode by using the in-situ measurements.

83 2. Methodology

84 2.1 Site information and instrumentation

85 The aerosol sampling site was situated on the roof (about 15m height above the
86 surface) of a laboratory building in the yard of the Institute of Atmospheric Physics

87 (IAP), Chinese Academy of Sciences, which was located between the 3rd and 4th ring
88 roads of northeast Beijing (Zhang et al., 2014).

89 An integrating nephelometer (Model 3563, TSI inc., Minnesota, USA) was used to
90 measure the total light scattering and hemispheric back scattering coefficients (for
91 angles between 7°~170°, respectively) of low RH aerosol at wavelengths of 450, 550
92 and 700nm, no size-selective inlets were used. The nephelometer was operated at 5L
93 min⁻¹ with data resolution of one minute. The calibration was conducted every month
94 with filtered air and CO₂ as prescribed by the manufacturer. Subsequently, the data
95 were corrected for truncation errors and the non-lambertian light source based on the
96 measured Ångström exponents (Anderson and Ogren, 1998). On average, the corrected
97 values were within 10% of the measured values. The mass concentration of PM₁₀ and
98 PM_{2.5} were measured by a Thermo TEOM 1400AB/8500 FDMS (Filter Dynamic
99 Measurement System). The mass concentration of PM₁ was determined using a
100 Thermo TEOM 1400.

101 The particle number-size distribution between 14nm and 2500nm diameter was
102 measured by a Scanning Mobility Particle Sizer (SMPS, TSI inc., Minnesota, USA),
103 comprising of a model TSI 3080 electrostatic classifier and a model TSI 3775
104 condensation particle counter (CPC), and an Aerodynamic Particle Sizer (APS, Model
105 3321, TSI inc., Minnesota, USA). The SMPS data covered the particle size range from
106 14nm to 533nm, and the APS covered from 542 nm to 2500nm. The size-dependent
107 diffusional and gravitational losses for the inlet line have been corrected by using the
108 empirical functions given by Willeke and Baron (1993). The data collected from these

109 two instruments were merged into one particle size spectrum matrix (14nm to 2500nm)
110 according to the **methods** of Liu et al. (2014) and Beddows et al. (2010).
111 The aerosol chemical composition was acquired using an Aerodyne High-Resolution
112 Time-of-Flight Aerosol Mass Spectrometer (HR-ToF-AMS, or AMS, Aerodyne
113 Research Inc., Billerica, MA, USA). The organic matter, sulfate, nitrate, ammonium
114 and chlorine in non-refractory submicron particle mass-size **distributions** (NR-PM₁)
115 were determined under V and W ion optical modes alternatively every 7.5 minutes.
116 Detailed information of data analysis, collection efficiency (CE) and relative ionization
117 efficiency of the instrument were introduced by Zhang et al. (2014). Simultaneously,
118 the gaseous pollutants (**e.g.**, NO, NO_x, CO, O₃ and SO₂) were measured using Thermo
119 instruments (series of 42i, 48i, 49i and 43i, respectively, Thermo Fisher Scientific,
120 Franklin, Massachusetts, USA). Detailed introduction and calibrations were given by
121 (Tang et al., 2012; Wang et al., 2014).
122 An automatic meteorological observation instrument (Milos520, Vaisala, Finland) was
123 used to obtain meteorological parameters (relative humidity, air temperature, wind
124 speed and direction). The time base for all data in the study **was** Beijing zone time
125 (UTC+8).

126 **3. Results and discussion**

127 **3.1 Aerosol mass concentration and meteorological parameters**

128 Figure 1 shows the mass concentrations of PM₁, PM_{1-2.5}, PM_{2.5-10} and mass
129 concentration ratios of PM₁/PM_{2.5}, PM_{2.5}/PM₁₀ during the period. The **average** mass

130 concentrations of PM_1 , $PM_{2.5}$ and PM_{10} are $99.1 \pm 67.1 \mu\text{g m}^{-3}$, $188.3 \pm 128.8 \mu\text{g m}^{-3}$ and
131 $265.2 \pm 157.1 \mu\text{g m}^{-3}$, indicative of the high level of aerosol pollution. The average
132 mass ratios of $PM_1/PM_{2.5}$ and $PM_{2.5}/PM_{10}$ are 0.56 ± 0.16 and 0.64 ± 0.15 , respectively.
133 As we can see in Figure 1(b), the mass ratio of $PM_1/PM_{2.5}$ is higher than that of
134 $PM_{2.5}/PM_{10}$ before January 28, indicating that PM_1 dominated the total mass. The
135 aerosol concentration increased gradually and reached the maximum values at 12:00 of
136 January 29, with PM_1 , $PM_{2.5}$ and PM_{10} values of $243.1 \mu\text{g m}^{-3}$, $504.6 \mu\text{g m}^{-3}$ and
137 $620.8 \mu\text{g m}^{-3}$. The detailed interpretations of the high values will be presented in
138 following section. Thereafter, the aerosol concentrations decreased rapidly to a lower
139 level. The mass ratios of $PM_1/PM_{2.5}$ and $PM_{2.5}/PM_{10}$ showed opposite pattern with
140 time variation during the period, indicating a decreasing fraction of PM_1 compared
141 with $PM_{2.5}$ and an increasing fraction of $PM_{2.5}$ compared with PM_{10} with increasing
142 aerosol pollution. It is worth noting that the increase of $PM_{1-2.5}$ was greatest during the
143 period January 28 to 29, as showed in Figure 1(a). Figure S1 displays meteorological
144 parameters during the episode. During this period, the average wind speed was 2.5
145 m/s. Figure S2 shows an overview of wind rose of the local wind and the wind is
146 mainly in the southerly and northerly quadrant, which can bring relative dirty or clean
147 air masses, respectively. Figure 2 exhibits 72 hours backward trajectories of air
148 parcels every 3 hours using Hysplit model from a height of 100m, with a total of six
149 clusters yielded (<http://ready.arl.noaa.gov/HYSPLIT.php>). We should clarify that the
150 southern area of Beijing often suffers more polluted atmosphere than that in northern
151 area due to more cities and population. The clusters of 1 to 5 are from northern

152 **direction**, with clean air and high transport height. **Furthermore**, long transport way
153 within 72 hours implies that those air parcels have a high transport speed compared
154 with cluster 6. The cluster 6, from southern and local **directions** with a fraction of
155 47%, has the **highest** frequency. The cluster has a **short transport distance of nearly**
156 **400 km**, low transport height and speed, resulting in a sufficient loading of surface air
157 pollutions compared with other clusters. We also present sounding data in Beijing
158 from university of Wyoming twice a day (<http://weather.uwyo.edu/upperair/>), as shown in
159 Figure 3. These lines with different **colors** represent sounding curves during the
160 observation period. It is worth noting that an inversion layer **between** 1000m to
161 1500m exists after January 27th. Particularly at 08:00 of 28th (Beijing time), the lapse
162 ratio of temperature is nearly **0.6°C/100m**, which means a very stable synoptic
163 condition. **Combined with low wind speed shown in figure S1, the horizontal motion**
164 **is also limited during the pollution episode.**

165 **3.2 Aerosol optical properties**

166 The aerosol scattering coefficient (σ_{sp}) and backscattering coefficient (σ_{bsp}) can be
167 directly measured by the nephelometer and then aerosol backscattering fraction (b_{λ}),
168 scattering Ångström exponent (\mathring{A}_{sp}) and asymmetry parameter (g_{λ}) can be calculated
169 **from the scattering coefficients, which** have rarely been reported in Beijing **using**
170 **in-situ** measurements. The aerosol light scattering coefficients show the same pattern
171 as mass concentration of PM, as shown in Figure 4. Table 1 shows the statistics of the
172 aerosol optical properties during this haze episode, **and** the average aerosol scattering
173 coefficients σ_{sp}^{450} , σ_{sp}^{550} and σ_{sp}^{700} are $1088.5 \pm 748.1 \text{ Mm}^{-1}$, $877.2 \text{ Mm}^{-1} \pm 624.2 \text{ Mm}^{-1}$

174 and $718.4 \text{ Mm}^{-1} \pm 530.8 \text{ Mm}^{-1}$, respectively. After converting the aerosol light
 175 scattering coefficients at 550nm to that of 525nm, the average σ_{sp} at 525nm are 3.2
 176 times greater than the yearly average values at another site in Beijing, reported by He
 177 et al. (2009). The average aerosol backscattering coefficients σ_{bsp}^{450} , σ_{bsp}^{550} and σ_{bsp}^{700} are
 178 $134.4 \text{ Mm}^{-1} \pm 87.1 \text{ Mm}^{-1}$, $108.1 \text{ Mm}^{-1} \pm 71.1 \text{ Mm}^{-1}$ and $98.7 \text{ Mm}^{-1} \pm 66.5 \text{ Mm}^{-1}$,
 179 respectively, as presented in Figure 4 (b). During the whole campaign, σ_{sp} and σ_{bsp}
 180 at three wavelengths were highly correlated. Both σ_{sp} and σ_{bsp} increase gradually
 181 from 24 to 29 January and decrease sharply to lower levels, which are consistent with
 182 the variations of aerosol mass concentrations.

183 The backscattering ratio, which is also called the hemispheric backscatter fraction, is
 184 the ratio of light scattered in the backward hemisphere to the total light scattered by
 185 particles. It is related to particle size distribution and can be calculated as following;

$$186 \quad b_{\lambda} = \frac{\sigma_{bsp}^{\lambda}}{\sigma_{sp}^{\lambda}} \quad (1)$$

187 The average b_{λ} at three wavelengths are 0.13 ± 0.02 , 0.14 ± 0.02 and 0.15 ± 0.02 ,
 188 respectively. A higher value of b_{λ} at 700nm indicates relatively more small size
 189 particles that scatter light in the backward hemisphere. The scattering Ångström
 190 exponent (\mathring{A}_{sp}) represents the wavelength dependence of scattering coefficient and is
 191 related to the slope of the number-size distribution or the mean size and relative
 192 concentrations of the accumulation and coarse mode aerosol. It is calculated using any
 193 two of three channels as following;

$$194 \quad \mathring{A} = - \frac{\log(\sigma_{sp}^{\lambda_1}) - \log(\sigma_{sp}^{\lambda_2})}{\log(\lambda_1) - \log(\lambda_2)} \quad (2)$$

195 The average $\overset{0}{A}_{450/550}$ and $\overset{0}{A}_{550/700}$ are 1.2 ± 0.3 and 0.94 ± 0.3 , respectively. The average
196 $\overset{0}{A}_{450/700}$ is 1.1 ± 0.3 , which is smaller than that of 1.46 in Guangzhou (Garland et al.,
197 2008) and 1.7 in Spain reported by (Titos et al., 2012), which indicates a more
198 dominant coarse mode particle compared with the other locations.

199 The asymmetry parameter g is a fundamental parameter for radiative transfer
200 calculation, and is defined as the intensity-weighted averaged cosine of the scattering
201 angle:

$$202 \quad g_{\lambda} = \frac{1}{2} \int_0^{\pi} \cos \theta P(\theta) \sin \theta d\theta \quad (3)$$

203 Where θ is the angle between incident light and scattering direction and $P(\theta)$ is the
204 angular distribution of scattered light (the phase function). The value of g_{λ} ranges
205 between -1 for completely backscattered light to +1 for completely forward scattered
206 light. Because there is no measurements can be directly obtained the values of g , a fit
207 equation applied by Andrews et al. (2006) was used as in equation 4.

$$208 \quad g_{\lambda} = -7.143889 * b_{\lambda}^3 + 7.464439 * b_{\lambda}^2 - 3.9356 * b_{\lambda} + 0.9893 \quad (4)$$

209 The average value of g_{λ} at 450nm, 550nm and 700nm are 0.58 ± 0.04 , 0.59 ± 0.05 and
210 0.54 ± 0.05 , respectively. The three parameters of b_{λ} , $\overset{\circ}{A}_{sp}$ and g_{λ} can show a relative
211 contribution of particle size to light scattering. During 24 and 25 January, b_{λ} and $\overset{\circ}{A}_{sp}$
212 shows higher values, which shows lower ones, as showed in Figure 4. However, the
213 opposite feature occurs when the haze developed. Especially during the highest
214 pollution periods (from 28 to 30 January), higher values of b_{λ} , $\overset{\circ}{A}_{sp}$ and lower values of
215 g_{λ} appear, which indicates an increasing fraction of relative coarse aerosol, consistent
216 with the variation pattern of $PM_1/PM_{2.5}$ showed in Figure 1(b).

217 3.3 particle number size distribution

218 The particle number-size distribution from January 25 to 31 is shown in Figure 5(a).
219 The particle number concentration peaks at a diameter of around 100 nm. These
220 particles are mainly from direct emissions of vehicles, cooking and new particle
221 formation (Shi et al., 2001). Particle volume concentration and mass concentration are
222 shown in figure 5(b) and (c), respectively, assuming an average aerosol bulk density
223 of 1.5 g.cm^3 and all particles are regular spheres based on the research by (Zhang et
224 al., 2004) in Pittsburgh PA, USA. The coarse mode particles between diameters of
225 1000nm to 2500nm increased significantly during the most heavily pollution periods
226 (28 and 29 January), as shown in Figure 5 (b) and 5 (c), which is consistent with
227 interpretations of variation ratio of $\text{PM}_{10}/\text{PM}_{2.5}$. The time series of calculated mass
228 concentration of $\text{PM}_{2.5}$, number concentrations of nucleation mode (14nm-25nm),
229 Aitken mode (25nm-100nm), accumulation mode (100nm-1000nm) and coarse mode
230 (1000 nm-2500nm) are presented in Figure 6. The calculated mass concentration of
231 $\text{PM}_{2.5}$ matches well with measured values, with R^2 values of 0.97, as shown in Figure
232 S3. The nucleation mode particles shows the highest number concentration during the
233 period, with an average value greater than $1.5 \times 10^6 \text{ cm}^{-3}$, indicating large emission of
234 reactive or low volatility, aerosol precursor gases (e.g. sulfur dioxide and organic
235 vapors). The lowest particle number concentration is in coarse mode ($D_m > 1000\text{nm}$),
236 with an average value of $3.18 \times 10^3 \text{ cm}^{-3}$. The Aitken mode and accumulation mode
237 also show high number concentrations, with the average values of $1.90 \times 10^5 \text{ cm}^{-3}$ and
238 $1.01 \times 10^6 \text{ cm}^{-3}$. Compared with three years of measurements of particle number

239 concentration at another urban site in Beijing, the number concentrations of
240 nucleation, Aitken and accumulation mode during this haze episode are more than 170
241 times, 10 times and 120 times, respectively (Hu et al., 2009). The nucleation mode
242 and Aitken mode particle **show** a significant increase at mid-day on 28 January, while
243 the accumulation mode **is not significant**. This may be **ascribed** to the emissions from
244 vehicle and cooking nearby our sampling site. It is worth noting that **the concentration**
245 **of coarse** mode particle was highest on the 28th and 29th of January, which is
246 consistent with the pattern of $PM_{2.5}/PM_{10}$. After the **coagulation, condensation and**
247 **hygroscopic growth**, the number concentrations of nucleation mode and Aitken mode
248 particle **decrease** on 12:00 of 30 January, as shown in Figure 6.

249 **3.4 aerosol chemical properties**

250 **The time series of** chemical compositions, mass fractions, O:C ratio and m/z 44 of
251 NR- PM_1 are presented in Figure7(a), (b) and (c). The average mass concentrations of
252 organic, sulfate, nitrate, ammonium and chloride are $62.1 \pm 46.1 \mu\text{g m}^{-3}$,
253 $28.4 \pm 22.1 \mu\text{g m}^{-3}$, $37.2 \pm 30.6 \mu\text{g m}^{-3}$, $17.4 \pm 12.7 \mu\text{g m}^{-3}$ and $5.5 \pm 4.2 \mu\text{g m}^{-3}$, **respectively**.
254 The organic component **is** dominant in NR- PM_1 , with an average mass fraction of
255 $44.9\% \pm 1.7\%$. Sulfate and nitrate species concentrations **are also very** high during the
256 **heavy haze event**.

257 AMS enables the real time determination of size-resolved chemical **compositions** of
258 different **mode particles** as a function of time. Figure 8 shows the temporal variations
259 of **the size distributions** of the organic (a), sulfate (b), nitrate (c), ammonium (d) and
260 chloride (e). The organic and chloride containing particles **display** a slightly broader

261 distribution than the other three species. All the aerosol components mainly reside in
262 the accumulation mode with vacuum aerodynamic diameters around 700nm. Note that
263 the AMS size distributions here are shown as a function of vacuum aerodynamic
264 diameter, D_{va} , which is the aerodynamic diameter measured under free-molecular
265 regime flow conditions. For a first approximation, 700nm in D_{va} corresponds roughly
266 to 470 nm in physical diameter of spherical particles. It is worth noting that particles
267 with optical diameters between 100nm and 1000nm have the highest scattering
268 efficiency in the visible range (Liou, 2002), so a high concentration at this optimum
269 aerosol size will lead to strong light scattering and worse visibility during the period.

270 These five aerosol components all show high concentrations from the afternoon of
271 28 January to noon of 29 January, corresponding with the highest mass loading and
272 light scattering of the whole pollution period. The detailed behaviors of particle
273 number concentration, size-resolved organic, sulfate, nitrate, ammonium and particle
274 mass concentration on January 28 are presented in Figure S5 and S6. The particle
275 number concentrations show a burst at nearly 12:00, with D_m less than 100nm.

276 Observations by Sakurai et al. (2005) in Atlanta, GA, USA recognized this as a plume
277 related to a new particle formation event, which was accompanied by advection of
278 local emissions. However, an increasing concentration of aerosol chemical
279 components at about 11:00 on 28 January is observed by AMS as shown in Figure S5.

280 The mass concentrations mainly reside on between 300nm and 1000nm in vacuum
281 diameter. This may be due to the accumulation of air pollutants under the stagnation
282 boundary layer. As we can see in figure S1, the meteorological parameters are

283 characterized by calm wind, low RH and increasing temperature in the morning,
284 which leads to a stable boundary layer. Then, with increasing surface temperature and
285 PBL height, the dilution causes the aerosol concentration **decreasing** in the afternoon.
286 The concentrations of sulfate, ammonium and nitrate **show** an increasing trend from
287 18:00. The major reasons are: (1) Increasing RH may enhance the heterogeneous
288 reaction of SO₂ and NH₃ to produce sulfate and nitrate. (2) Decreased PBL height at
289 night leads to accumulation of air pollutant. (3) **Conversion of N₂O₅ to nitrate via**
290 **heterogenous or homogenous ways and reaction of OH and NO₂ (Kim et al., 2014).**
291 All of the above aspects **result** in the mass concentrations of **nitrate** and ammonium
292 **have** a distinct growth **of particles** with **diameters** between 100nm and 500nm on 28
293 January.

294 **3.5 Increased formation of Secondary Organic Aerosol (SOA) during haze** 295 **pollution episode**

296 Figure 10 shows the **variations** of signal of m/z 44 as a function of organic
297 aerosol mass concentration and the influence of relative humidity. The frequency
298 distributions of organic mass and m/z 44 during the period are presented as well.
299 The highest occurrence of organic aerosol concentration **appears** nearly **between**
300 20 to 35μg m⁻³, corresponding with signal fraction of m/z 44 **less than** 2. The
301 signal of m/z 44 **shows** an increasing trend with increasing organic mass. The
302 lower concentration of organic component mainly **exists** at RH below 40%,
303 which **is** indicative of a relatively clean atmosphere in urban Beijing. It **is**
304 notable that the higher levels of the organic component **occurs** under high RH

305 conditions, of which aerosol water uptake ability is enhanced and the more
306 highly hydrated particles are able to capture more water-soluble volatile organic
307 compounds (VOCs). In this way, the dry mass concentration of organic aerosol
308 increases after the water evaporated in the AMS. The studies of Ge et al. (2012)
309 in central valley of California and Dall'Osto et al. (2009) in London also showed
310 that aqueous-phase processes are responsible for the production of secondary
311 organic aerosol species, most significantly during fog events.

312 **3.6 Light scattering apportionment**

313 Light scattering by atmospheric aerosols is highly dependent on their size,
314 morphology and compositions (Liou, 2002). Sulfate, nitrate, ammonium and organic
315 components in aerosol contribute most to light scattering, and particularly for
316 diameters ranging from 100nm to 1000nm, they have the greatest light extinction
317 efficiency (Seinfeld and Pandis, 1998). Here, a modified IMPROVE algorithm was
318 employed to apportion light scattering coefficients at $\lambda=550\text{nm}$ (Pitchford et al., 2007).
319 The IMPROVE algorithm was based on a multiple linear regression method (Chan et
320 al., 1999), which considers the degree to which aerosol light scattering is related to
321 the mass concentration of each component combined with water uptake of inorganic
322 component. The detailed introduction of the method can be found in
323 Lowenthal et al. (1995). The $f(\text{RH})$ curve obtained by Chen et al. (2014) during
324 January in Northern China Plain is used here.

325 In our light apportionment calculation, the mass concentrations of ammonium sulfate,
326 ammonium bisulfate, ammonium nitrate, ammonium chloride and organic were

327 required. However, the AMS can only provide us **with** mass concentrations of sulfate,
328 nitrate, ammonium chloride and organic compounds. Here, a commonly accepted ion
329 pairing scheme of calculating the neutral aerosol from the molar number of all ions
330 simplified by Gysel et al. (2007) is applied. In this scheme, by setting the fraction of
331 nitric acid to zero, the molar fraction of ammonium nitrate is equal to the molar
332 fraction of nitrate ions. The rest of ammonium ions are assigned **to ammonium**
333 **bisulfate, ammonium sulfate** and ammonium chloride according to ammonium molar
334 fraction.

335 In IMPROVE algorithm, the light scattering growth due to inorganic components
336 were considered, while the contribution from organic aerosol **did not take into account**.
337 Then, using the highly resolution mass concentrations of **sulfate containing aerosol,**
338 ammonium nitrate, ammonium chloride and organic in submicron aerosol and aerosol
339 scattering growth curve, we get a relationship of scattering coefficient and aerosol
340 components and light scattering growth factor as showed in formula 9 . The fitting
341 was finished under MATLAB software (MATLAB R2010a). Figure 11 (a) shows the
342 time series of apportioned light scattering coefficients of each aerosol components
343 compared with measured values during observation period. At the beginning of the
344 periods, organic component dominated light scattering. With the development of the
345 haze, the contribution of inorganic components increased as shown in Figure 11 (b).
346 The total average light scattering contribution of each aerosol component is presented
347 in Figure 12. The apportionment contributions from organic, **sulfate,** ammonium
348 nitrate and ammonium chloride were **54%, 24%, 12% and 10%**, respectively, which

349 indicated the dominant contribution of organic and sulfate compounds to light
350 scattering during this haze episode in Beijing. One should note that the apportioned
351 light scattering coefficient using IMPROVE method is highly related with its mass
352 concentration, and organic aerosol has a large mass fractions in it. Yao et al. (2010)
353 showed that the organic components contributed greatly to the light extinction (about
354 45% contribution) by using AMS data during winter in Shenzhen, PRC. Watson (2002)
355 also found the organic aerosol dominated light extinction in some cities, with
356 fractions of 9% ~50% in east USA.

$$\begin{aligned} \sigma_{sp}^{550} = & 6.5 f(RH)[(NH_4)_2SO_4] + 6.5 f(RH)[NH_4HSO_4] + 2.2 f(RH)[NH_4NO_3] \\ & + 4.3 f(RH)[NH_4Cl] + 5.7[organic] + 57.3 \end{aligned} \quad (9)$$

358 **4. Summary and Conclusion**

359 Based on in-situ measurements, the physical and chemical properties of aerosol
360 particles were characterized during a severe haze episode in Beijing from 24 January
361 to 31 January during, 2013. The average mass concentrations of PM₁, PM_{2.5} and PM₁₀
362 were 99.1 ± 67.1 μg m⁻³, 188.3 ± 128.8 μg m⁻³ and 265.2 ± 157.1 μg m⁻³, respectively, and
363 an increasing fraction of PM_{1-2.5} was significant during the most heavy pollution
364 periods. The averaged scattering coefficient at 550 nm was 877.2 Mm⁻¹ ± 624.2 Mm⁻¹,
365 and an increasing amount of relative coarse particle also can be seen from the
366 variations of backscattering ratios, asymmetry parameter and scattering Ångström
367 exponent. Particle number size distribution (14 nm to 2500 nm) showed high number
368 concentrations in the nucleation and accumulation modes. Size-resolved chemical
369 composition of submicron aerosol from a HR-ToF-AMS showed that the mass
370 concentration of organic, sulfate, nitrate, ammonium and chlorine mainly resided on

371 500nm-800nm in vacuum diameter, and sulfate and ammonium contributed to **the**
372 **growth** of particle during the most heavily polluted day on January 28.
373 High emissions of **background pollutant** combined with stable synoptic conditions
374 and increasing of relative humidity, which lead to enhanced water uptake ability of
375 submicron aerosol and formation of secondary aerosol, may be the main reasons for
376 the heavy haze episode. Light scattering apportionment showed that organic, **sulfate**
377 **containing components**, ammonium nitrate and ammonium chloride contributed to
378 light scattering fractions of **54%, 24%, 12% and 10%**, respectively. Considering their
379 dominant fractional contribution to light scattering and light extinction, our study
380 indicated that organic components also play an important role in visibility degradation
381 **during** the winter haze episode in Beijing.

382 **Acknowledgment**

383 We acknowledge Professor Zhang Wu of Lanzhou University for help in nephelometer
384 maintaining. **We also acknowledge NOAA, university of Wyoming for backward**
385 **trajectory soft and meteorological data analysis, respectively.** This work was supported
386 by National Natural Science Foundation of China (41230642), the CAS Strategic
387 Priority Research Program grant XDA05100100 and XDB05020402.

388 **Reference**

389 Anderson, T.L. et al., 2003. Atmospheric science. Climate forcing by aerosol--a hazy picture. *Science*,
390 300(5622): 1103-4.
391 Anderson, T. L., and Ogren, J. A.: Determining Aerosol Radiative Properties Using
392 the Tsi 3563 Integrating Nephelometer, *Aerosol Science and Technology*, 29, 57-
393 69, 10.1080/02786829808965551, 1998

394 Andrews, E. et al., 2006. Comparison of methods for deriving aerosol asymmetry parameter. *Journal of*
395 *Geophysical Research*, 111(D5).

396 Beddows, D.C.S., Dall'osto, M. and Harrison, R.M., 2010. An Enhanced Procedure for the Merging of
397 Atmospheric Particle Size Distribution Data Measured Using Electrical Mobility and
398 Time-of-Flight Analysers. *Aerosol Science and Technology*, 44(11): 930-938.

399 Chan, Y.C. et al., 1999. Source apportionment of visibility degradation problems in Brisbane (Australia)
400 using the multiple linear regression techniques. *Atmospheric Environment*, 33(19):
401 3237-3250.

402 Chen, J. et al., 2012. A parameterization of low visibilities for hazy days in the North China Plain.
403 *Atmospheric Chemistry and Physics*, 12(11): 4935-4950.

404 Chen, J., Zhao, C.S., Ma, N. and Yan, P., 2014. Aerosol hygroscopicity parameter derived from the
405 light scattering enhancement factor measurements in the North China Plain. *Atmos. Chem.*
406 *Phys.*, 14(15): 8105-8118.

407 Cheng, Y.F. et al., 2012. Size-resolved measurement of the mixing state of soot in the megacity Beijing,
408 China: diurnal cycle, aging and parameterization. *Atmospheric Chemistry and Physics*, 12(10):
409 4477-4491.

410 Dall'Osto, M., Harrison, R.M., Coe, H. and Williams, P., 2009. Real-time secondary aerosol formation
411 during a fog event in London. *Atmos. Chem. Phys.*, 9(7): 2459-2469.

412 Deng, Z.Z. et al., 2013. Examination of parameterizations for CCN number concentrations based on
413 in-situ aerosol activation property measurements in the North China Plain. *Atmospheric*
414 *Chemistry and Physics Discussions*, 13(1): 145-176.

415 Garland, R.M. et al., 2008. Aerosol optical properties in a rural environment near the mega-city
416 Guangzhou, China: implications for regional air pollution, radiative forcing and remote
417 sensing. *Atmos. Chem. Phys.*, 8(17): 5161-5186.

418 Ge, X., Zhang, Q., Sun, Y., Ruehl, C.R. and Setyan, A., 2012. Effect of aqueous-phase processing on
419 aerosol chemistry and size distributions in Fresno, California, during wintertime.
420 *Environmental Chemistry*, 9(3): 221.

421 Gysel, M. et al., 2007. Closure study between chemical composition and hygroscopic growth of aerosol
422 particles during TORCH2. *Atmos. Chem. Phys.*, 7(24): 6131-6144.

423 He, X. et al., 2009. An intensive study of aerosol optical properties in Beijing urban area. *Atmos. Chem.*
424 *Phys.*, 9: 8903-8915

425 Hu, M., He, L., Huang, X. and Wu, Z.; Chemical and physical properties, source and
426 formation of fine and ultrafine particle in Beijing, Science Press, 2009.

427 Huang, K. et al., 2010a. Relation between optical and chemical properties of dust aerosol over Beijing,
428 China. *Journal of Geophysical Research*, 115.

429 Huang, X.F. et al., 2010b. Highly time-resolved chemical characterization of atmospheric submicron
430 particles during 2008 Beijing Olympic Games using an Aerodyne High-Resolution Aerosol
431 Mass Spectrometer. *Atmospheric Chemistry and Physics*, 10(18): 8933-8945.

432 Kaufman, Y.J., Koren, I., Remer, L.A., Rosenfeld, D. and Rudich, Y., 2005. The effect of smoke, dust,
433 and pollution aerosol on shallow cloud development over the Atlantic Ocean. *Proc Natl Acad*
434 *Sci U S A*, 102(32): 11207-12.

435 Koren, I., Kaufman, Y.J., Rosenfeld, D., Remer, L.A. and Rudich, Y., 2005. Aerosol invigoration and

436 restructuring of Atlantic convective clouds. *Geophysical Research Letters*, 32(14): n/a-n/a.

437 Li, W.J., Shao, L.Y. and Buseck, P.R., 2010. Haze types in Beijing and the influence of agricultural
438 biomass burning. *Atmospheric Chemistry and Physics*, 10(17): 8119-8130.

439 Liu, X.G. et al., 2013. Formation and evolution mechanism of regional haze: a case study in the
440 megacity Beijing, China. *Atmospheric Chemistry and Physics*, 13(9): 4501-4514.

441 Liu, Z. et al., 2015. Seasonal and diurnal variation in particulate matter (PM₁₀ and PM_{2.5}) at an urban
442 site of Beijing: analyses from a 9-year study. *Environmental Science and Pollution Research*,
443 22(1): 627-642.

444 Liu, Z.R., Hu, B., Liu, Q., Sun, Y. and Wang, Y.S., 2014. Source apportionment of urban fine particle
445 number concentration during summertime in Beijing. *Atmospheric Environment*(0).

446 Lohmann, U. and Feichter, a.J., 2005. Global indirect aerosol effects: a review. *Atmos. Chem. Phys.*
447 , 5: 715-737.

448 Liou, K.N.: *An introduction to atmospheric radiation (second edition)* , Elsevier
449 Science, 2002.

450 Lowenthal, D.H., Rogers, C.F., Saxena, P., Watson, J.G. and Chow, J.C., 1995. Sensitivity of estimated
451 light extinction coefficients to model assumptions and measurement errors. *Atmospheric*
452 *Environment*, 29(7): 751-766.

453 Ma, N. et al., 2012. A new method to determine the mixing state of light absorbing carbonaceous using
454 the measured aerosol optical properties and number size distributions. *Atmospheric Chemistry*
455 *and Physics*, 12(5): 2381-2397.

456 Meier, J. et al., 2009. Hygroscopic growth of urban aerosol particles in Beijing (China)
457 during wintertime: a comparison of three experimental methods. *Atmos. Chem. Phys.*, , 9: 6865–6880
458

459 Nel, A., 2005. Atmosphere. Air pollution-related illness: effects of particles. *Science*, 308(5723): 804-6.

460 Pan, X.L. et al., 2009. Observational study of influence of aerosol hygroscopic growth on scattering
461 coefficient over rural area near Beijing mega-city. *Atmos. Chem. Phys.*
462 , 9: 7519–7530.

463 Pitchford, M. et al., 2007. Revised Algorithm for Estimating Light Extinction from IMPROVE Particle
464 Speciation Data. *Journal of the Air & Waste Management Association*, 57(11): 1326-1336.

465 Poschl, U., 2005. Atmospheric aerosols: composition, transformation, climate and health effects.
466 *Angew Chem Int Ed Engl*, 44(46): 7520-40.

467 Qu, W.J. et al., 2010. Spatial distribution and interannual variation of surface PM₁₀
468 concentrations over eighty-six Chinese cities. *Atmospheric Chemistry and Physics*, 10(12):
469 5641-5662.

470 Quan, J. et al., 2011. Analysis of the formation of fog and haze in North China Plain (NCP).
471 *Atmospheric Chemistry and Physics*, 11(15): 8205-8214.

472 Ramanathan, V., Crutzen, P.J., Kiehl, J.T. and Rosenfeld, D., 2001. Aerosols, climate, and the
473 hydrological cycle. *Science*, 294(5549): 2119-24.

474 Sakurai, H. et al., 2005. Hygroscopicity and volatility of 4–10 nm particles during summertime
475 atmospheric nucleation events in urban Atlanta. *Journal of Geophysical Research*:
476 *Atmospheres*, 110(D22): D22S04.

477 Seinfeld, J. H., and Pandis, S. N.: *Atmospheric Chemistry and physics, From Air*

478 Pollution to Climate Changes, Wiley, New York, USA, 1998.

479 Shi, J.P., Evans, D.E., Khan, A.A. and Harrison, R.M., 2001. Sources and concentration of
480 nanoparticles ($10\text{--}100\text{ nm}$ diameter) in the urban atmosphere. *Atmospheric Environment*,
481 35(7): 1193-1202.

482 Sun, Y.L., Zhuang, G.S., Tang, A., Wang, Y. and And An, Z., 2006. Chemical Characteristics of
483 PM_{2.5} and PM₁₀ in Haze-fog Episodes in Beijing. *Environ. Sci. Technol.*, 40: 3148-3155.

484 Tang, G. et al., 2012. Spatial-temporal variations in surface ozone in Northern China as observed
485 during 2009–2010 and possible implications for future air quality control strategies. *Atmos.*
486 *Chem. Phys.*, 12(5): 2757-2776.

487 Titos, G. et al., 2012. Optical properties and chemical composition of aerosol particles at an urban
488 location: An estimation of the aerosol mass scattering and absorption efficiencies. *Journal of*
489 *Geophysical Research: Atmospheres*, 117(D4): D04206.

490 Twomey, S., 1977. The Influence of Pollution on the Shortwave Albedo of Clouds. *Journal of the*
491 *Atmospheric Sciences*, 34: 1149-1152.

492 Wang, K.C., Dickinson, R.E., Su, L. and Trenberth, K.E., 2012a. Contrasting trends of mass and optical
493 properties of aerosols over the Northern Hemisphere from 1992 to 2011. *Atmospheric*
494 *Chemistry and Physics*, 12(19): 9387-9398.

495 Wang, L. et al., 2012b. Understanding haze pollution over the southern Hebei area of China using the
496 CMAQ model. *Atmospheric Environment*, 56: 69-79.

497 Wang, Y. et al., 2013. Mechanism for the formation of the January 2013 heavy haze pollution episode
498 over central and eastern China. *Science China Earth Sciences*.

499 Wang, Y.H. et al., 2014. Ozone weekend effects in the Beijing–Tianjin–Hebei metropolitan area, China.
500 *Atmos. Chem. Phys.*, 14(5): 2419-2429.

501 Watson, J.G., 2002. Visibility: Science and Regulation. *Journal of the Air & Waste Management*
502 *Association*, 52(6): 628-713.

503 Wehner, B. et al., 2008. Relationships between submicrometer particulate air pollution and
504 air mass history in Beijing, China, 2004–2006. *Atmos. Chem. Phys.*, 8: 6155–6168.

505 Wu, Z. et al., 2007. New particle formation in Beijing, China: Statistical analysis of a 1-year data set.
506 *Journal of Geophysical Research*, 112(D9).

507 Yang, M., Howell, S.G., Zhuang, J. and Huebert, a.B.J., 2009. Attribution of aerosol light absorption to
508 black carbon, brown
509 carbon, and dust in China – interpretations of atmospheric
510 measurements during EAST-AIRE. *Atmos. Chem. Phys.*, 9: 2035–2050.

511 Yao, T. et al., 2010. High time resolution observation and statistical analysis of atmospheric light
512 extinction properties and the chemical speciation of fine particulates. *SCIENCE CHINA*
513 *Chemistry*, 53(8): 1801-1808.

514 Zhang, J.K. et al., 2014. Characterization of submicron aerosols during a month of serious pollution in
515 Beijing, 2013. *Atmos. Chem. Phys.*, 14(6): 2887-2903.

516 Zhang, Q., Quan, J., Tie, X., Huang, M. and Ma, X., 2011. Impact of aerosol particles on cloud
517 formation: Aircraft measurements in China. *Atmospheric Environment*, 45(3): 665-672.

518 Zhang, Q. et al., 2004. Insights into the Chemistry of New Particle Formation and Growth Events in
519 Pittsburgh Based on Aerosol Mass Spectrometry. *Environmental Science & Technology*,
520 38(18): 4797-4809.

521 Zhang, Q.H., Zhang, J.P. and Xue, H.W., 2010. The challenge of improving visibility in Beijing.
522 Atmospheric Chemistry and Physics, 10(16): 7821-7827.

523 Zhang, X. et al., 2013. Factors contributing to haze and fog in China. Chinese Science Bulletin
524 (Chinese Version), 58(13): 1178.

525 Zhang, X.Y. et al., 2012. Atmospheric aerosol compositions in China: spatial/temporal variability,
526 chemical signature, regional haze distribution and comparisons with global aerosols.
527 Atmospheric Chemistry and Physics, 12(2): 779-799.

528 Zhao, X.J. et al., 2013. Analysis of a winter regional haze event and its formation mechanism in the
529 North China Plain. Atmospheric Chemistry and Physics, 13(11): 5685-5696.

530

531

532

533

534

535

536

537

538

539

540

541

542

543

544

545

546

547

548

549 Table 1 The statistic of aerosol optical properties during observation period.

Parameter	mean	median	Standard derivation	5% quantile	95% quantile
σ_{sp}^{450} (Mm ⁻¹)	1088.5	924.4	748.1	48.1	2386.3
σ_{sp}^{550} (Mm ⁻¹)	877.2	748.4	624.2	36.6	1993.4
σ_{sp}^{700} (Mm ⁻¹)	718.4	628.2	530.9	28.7	1703.3
σ_{bsp}^{450} (Mm ⁻¹)	134.4	122.8	87.1	7.6	281.4
σ_{bsp}^{550} (Mm ⁻¹)	108.1	96.4	71	6.1	228.5
σ_{bsp}^{700} (Mm ⁻¹)	98.7	89.3	66.5	7.3	214.4
b_{450}	0.13	0.13	0.02	0.11	0.16
b_{550}	0.14	0.12	0.02	0.11	0.17
b_{700}	0.15	0.14	0.02	0.13	0.19
$A_{450/550}^0$	1.2	1.3	0.3	0.74	1.7
$A_{550/700}^0$	0.94	1.0	0.3	0.41	1.4
g_{450}	0.58	0.6	0.04	0.52	0.62
g_{550}	0.57	0.6	0.05	0.50	0.63
g_{700}	0.54	0.56	0.05	0.46	0.60

550

551

552 Table 2 The statistic of particle number concentration during observation period.

Parameter	Mean	median	Standard derivation	5% quantile	95% quantile
Nucleation(cm^{-3})	1.90×10^5	1.8×10^5	8.3×10^4	6.3×10^4	3.4×10^5
Aitken(cm^{-3})	1.5×10^6	1.4×10^6	6.4×10^5	5.7×10^5	2.7×10^6
Accumulation(cm^{-3})	1×10^6	9.9×10^6	3.9×10^5	4.7×10^5	1.6×10^6
Coarse (cm^{-3})	3.1×10^3	2.9×10^3	2.3×10^3	2.5×10^2	7.0×10^3

553

554

555

556

557

558

559

560

561

562

563

564

565

566

567

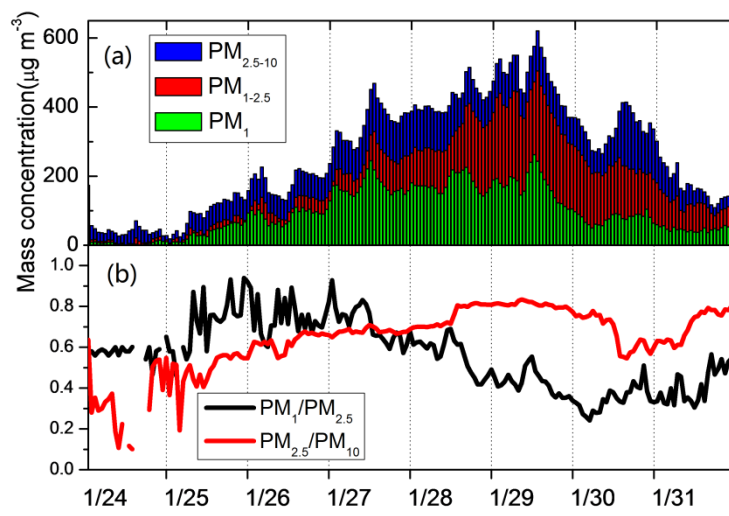


Figure 1 Time series of (a) mass concentrations of PM_1 , $\text{PM}_{1-2.5}$ and $\text{PM}_{2.5-10}$, (b) mass ratios of $\text{PM}_1/\text{PM}_{2.5}$ and $\text{PM}_{2.5}/\text{PM}_{10}$

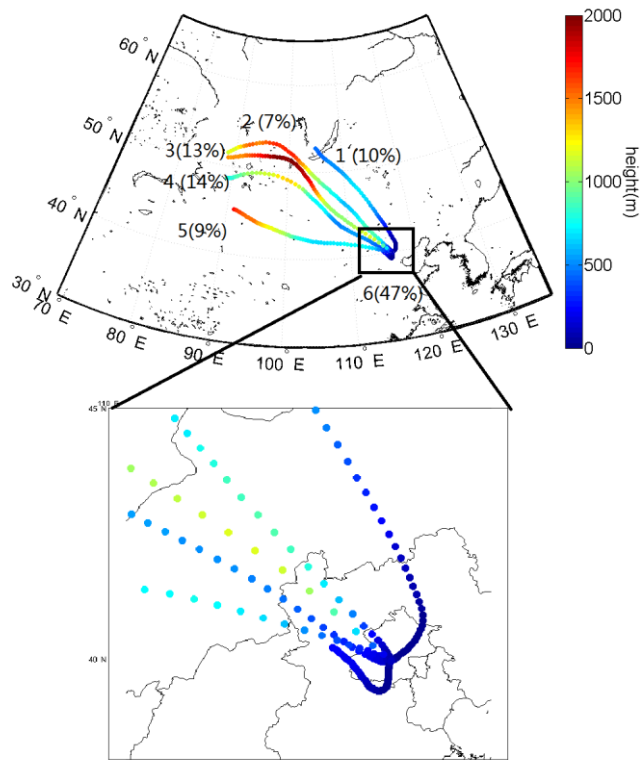


Figure 2 The three days backward trajectory of air parcels during the observation period; the colors of air trajectories represent height during transport.

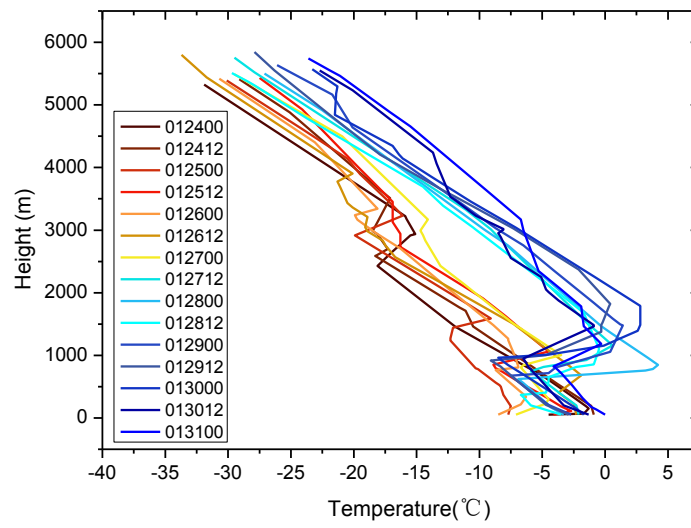


Figure 3 The temperature profiles during observation period. The legend stands for UTC time. For example, 012400 means 0:00 on January 24th.

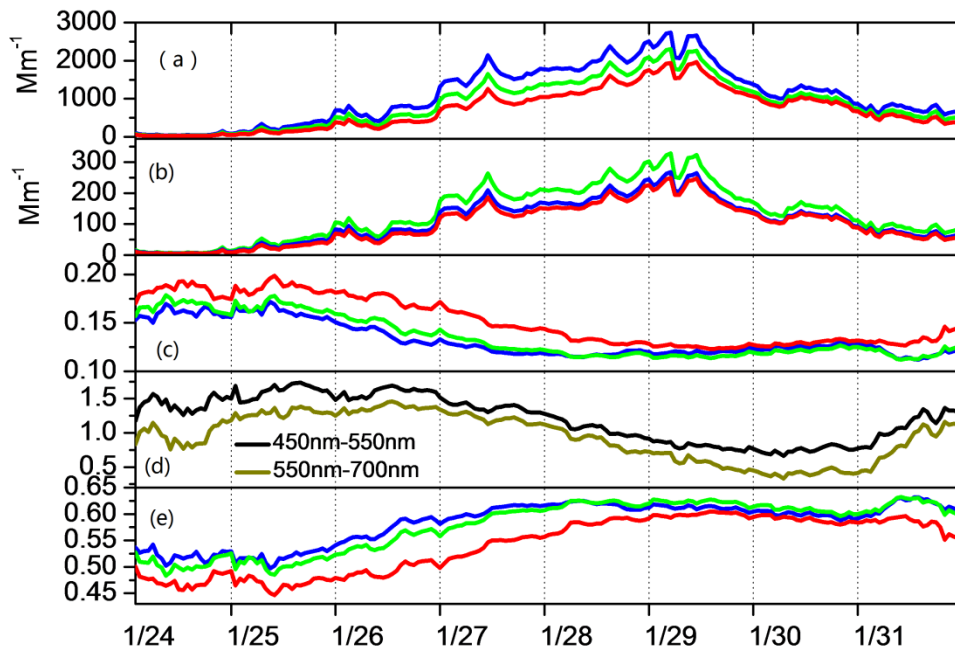


Figure 4 Time series of (a) scattering coefficients σ_{sp} , (b) backscattering coefficients σ_{bsp} , (c) backscattering ratios b_{λ} , (e) asymmetry parameter g_{λ} at wavelengths of 450nm (blue), 550nm (green) and 700nm (red) (d) scattering Ångström exponent (\AA_{sp}) from 450nm-550nm (black) and 550nm-700nm(brown).

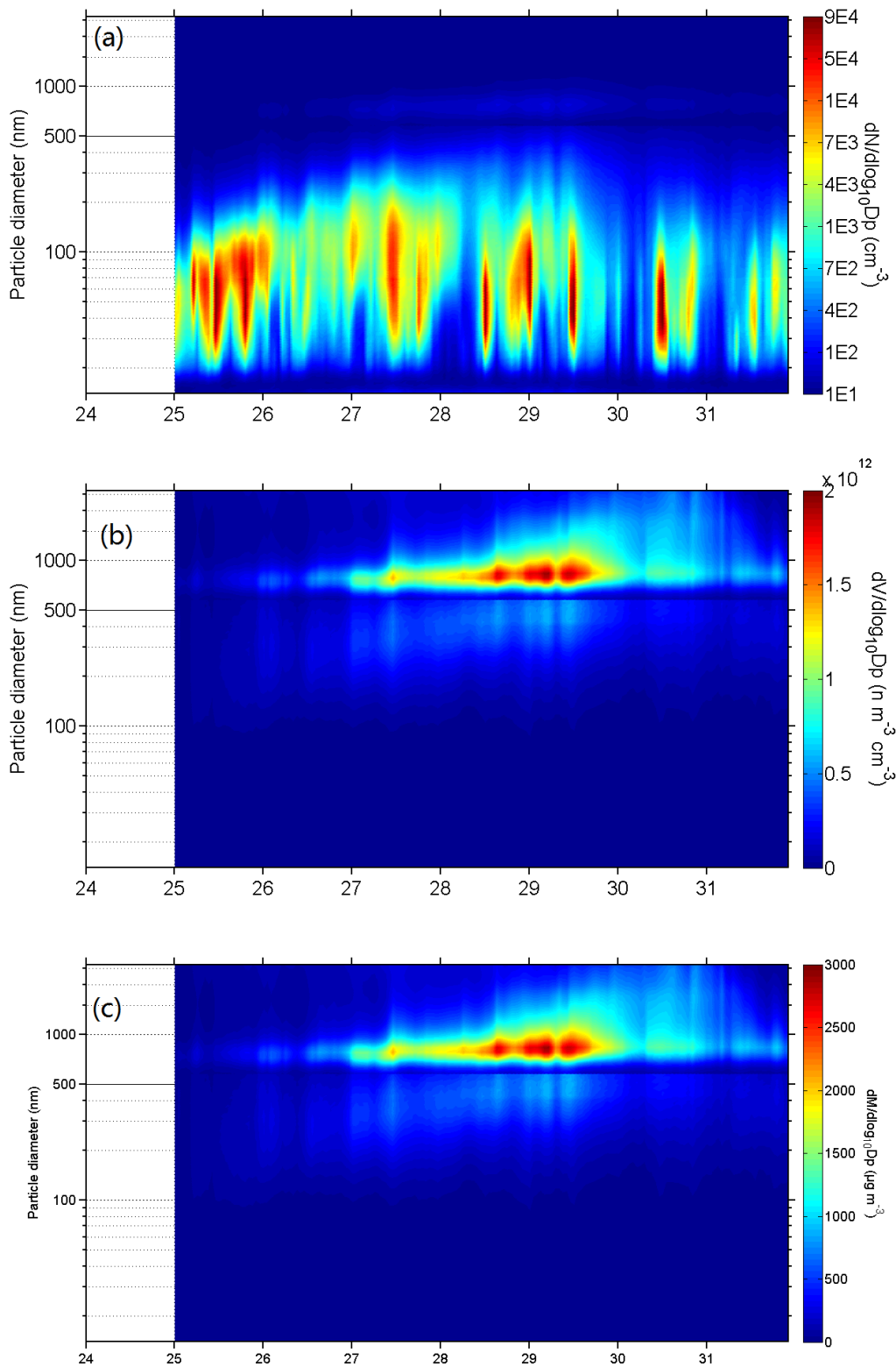


Figure 5 Time series of (a) particle number size distribution (b) particle volume size distribution (c) particle mass size distribution between 14.1nm-2458nm using SMPS combined with APS from January 25 to 31. The x-axis represents the data of January

and y-axis represents particle diameter (nm). The color in the figure 3 represents particle concentration ($dN/d\log D_p$).

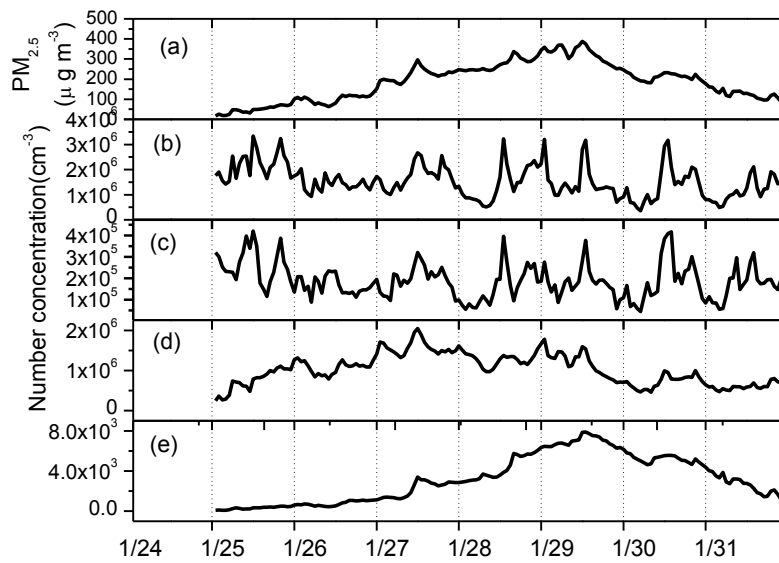


Figure 6 Time series of (a) particle mass concentration calculated from number size distribution and number concentrations of (b) nucleation mode (14.1nm-25nm), (c) Aitken mode (25nm-100nm), (d) accumulation mode (100nm-1000nm) and (e) coarse mode (1000nm-2458nm) from January 25 to January 31.

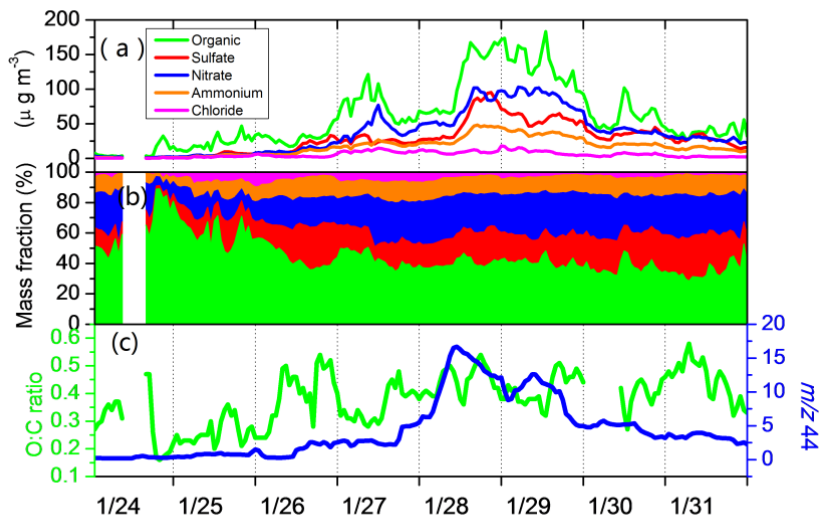
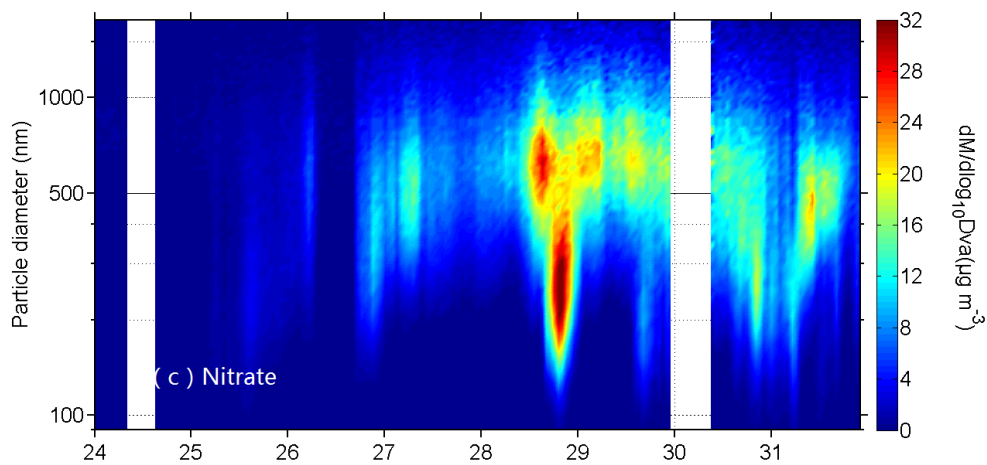
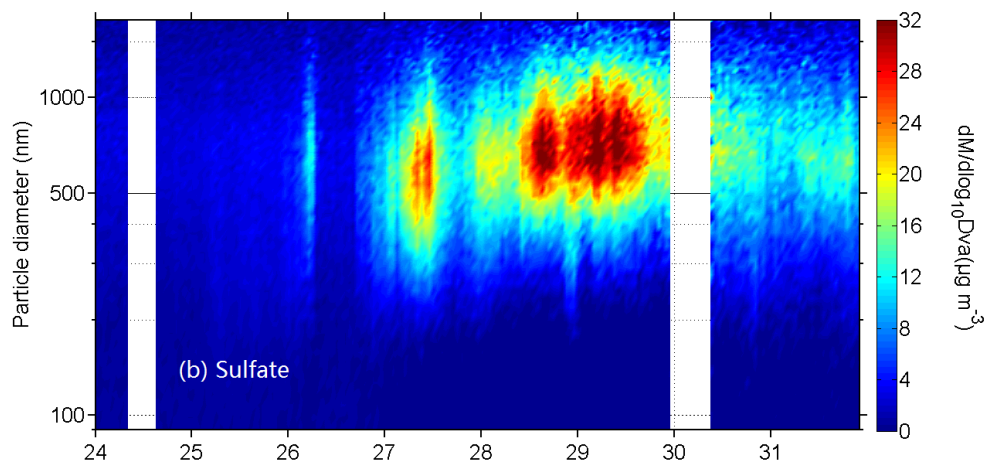
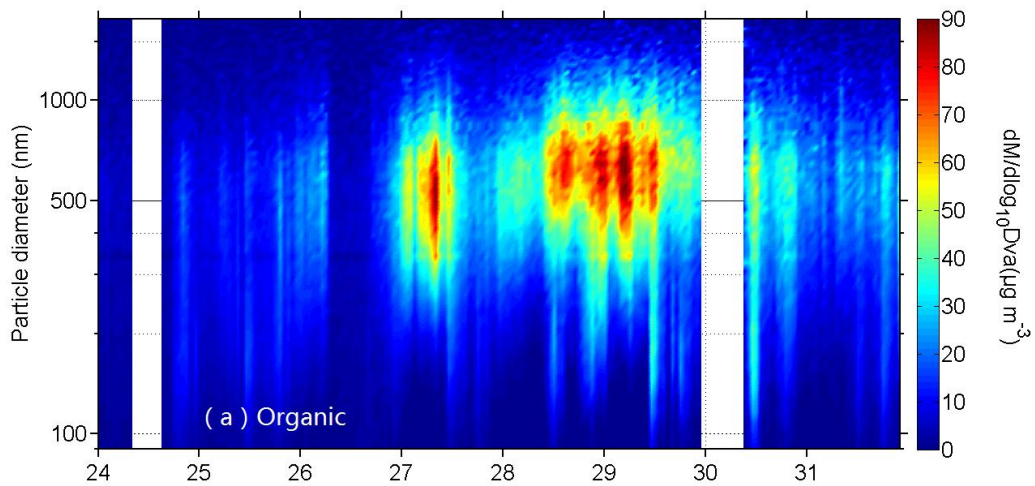


Figure 7 Time series of (a) mass concentrations of organic, sulfate, nitrate, ammonium and chloride in submicron aerosol (b) mass fractions of organic, sulfate, nitrate, and ammonium and chloride (c) O: C ratio and m/z 44 during the haze episode.



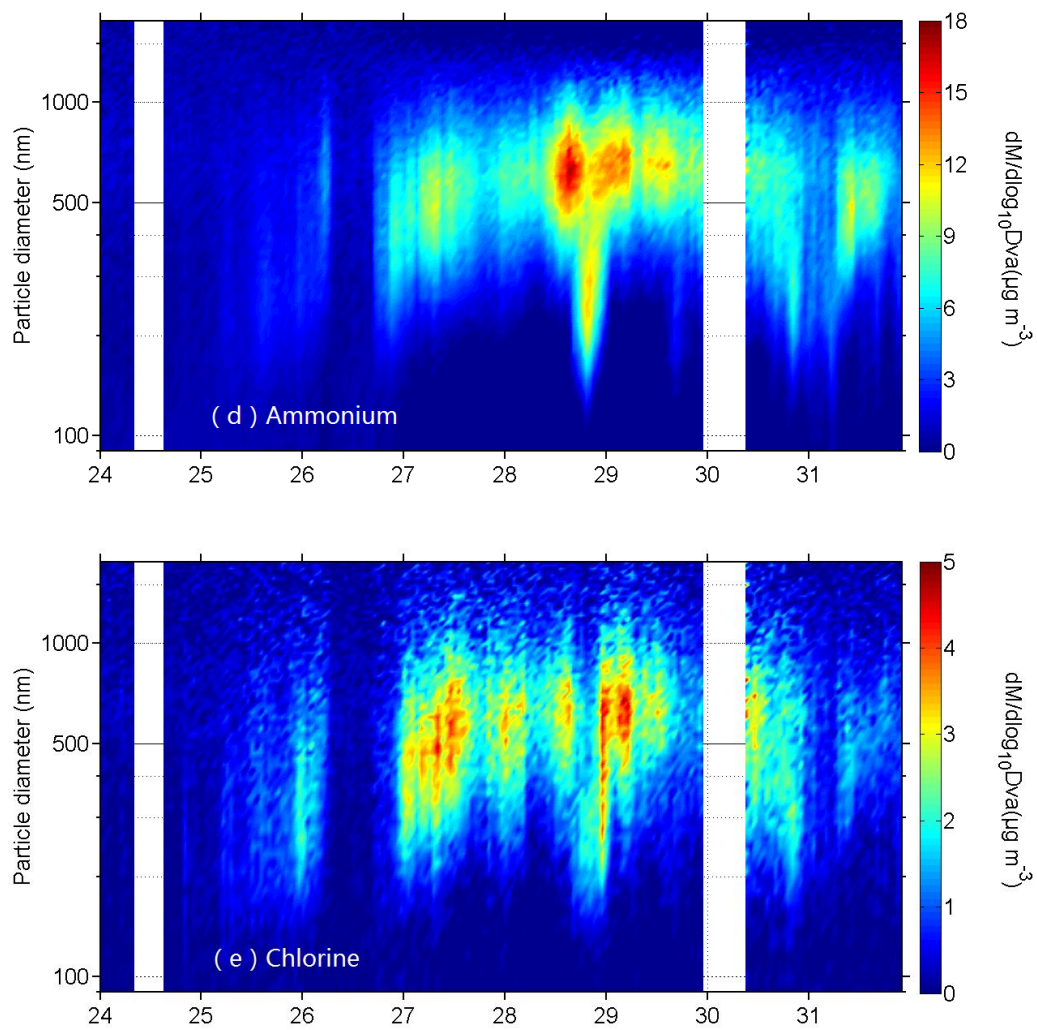


Figure 8 Size-resolved chemical compositions of (a) organic (b) sulfate (c) nitrate (d) ammonium and (e) chlorine

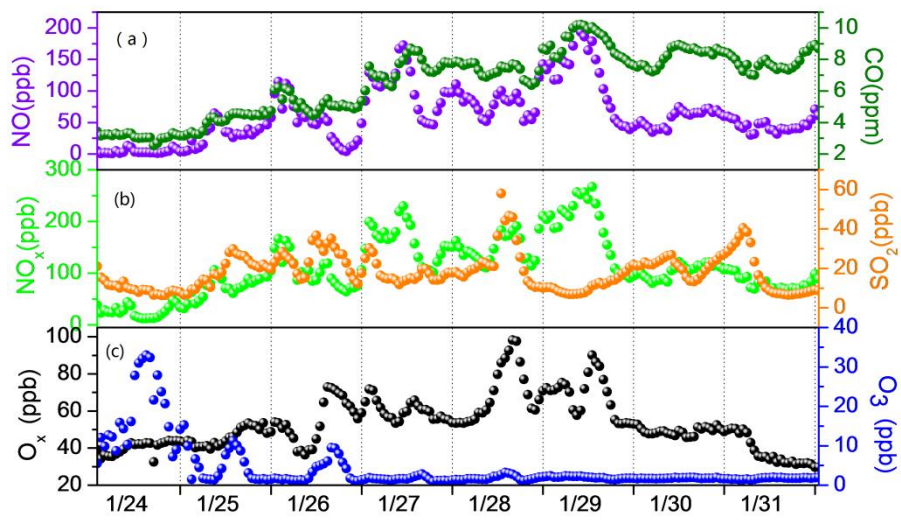


Figure 9 Mixing ratios of (a) NO and CO (b) NO_x and SO₂ (c) O_x and O₃

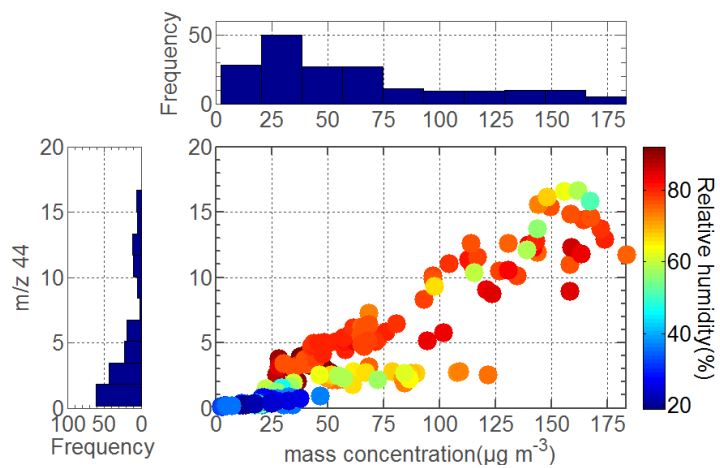


Figure 10 (left panel) the frequency distribution of m/z 44, (top panel) the frequency distribution of organic mass, (center panel) abundance of m/z 44 as a function of organic aerosol mass concentration and the influence of RH (left, color scale).

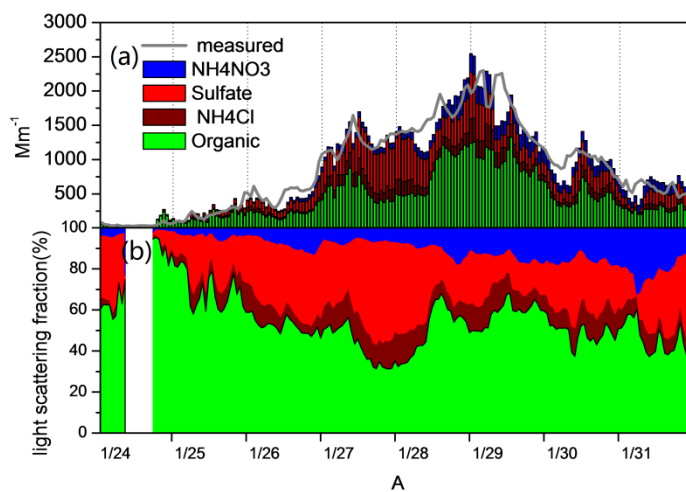


Figure 11 Time series of (a) apportioned light scattering coefficients of each aerosol components compared with measured (b) light scattering fractions of each aerosol components.

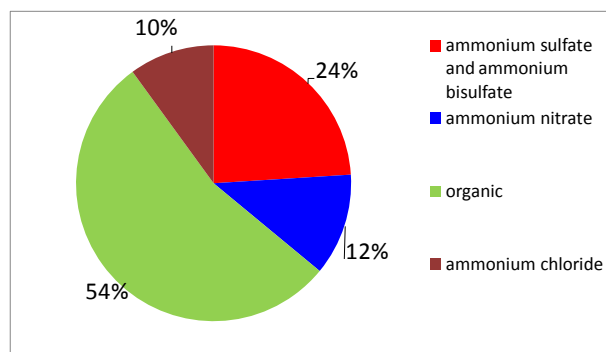


Figure 12 Averaged light scattering contribution of each aerosol components during the haze episode